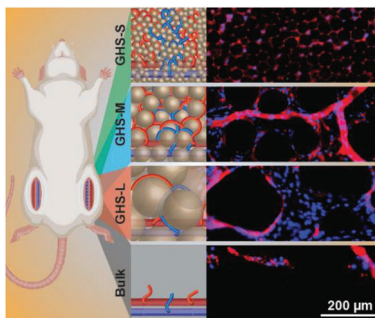# RESEARCH ARTICLES

Z. Ataie, S. Horchler, A. Jaberi,
S. V. Koduru, J. C. El-Mallah, M. Sun,
S. Kheirabadi, A. Kedzierski,
A. Risbud, A. R. A. E Silva,
D. J. Ravnic,* A. Sheikhi* 2307928

**Accelerating Patterned Vascularization
Using Granular Hydrogel Scaffolds
and Surgical Micropuncture**

GHS-S

GHS-M

GHS-L

Bulk

200 μm

Coordinated engineering (granular hydrogel scaffold) and surgical (micropuncture) approaches yield rapidly vascularized scaffolds with controllable microvascular patterns that may enable the development of new and translatable reconstructive and regenerative therapeutics.

Accelerating Patterned Vascularization Using Granular Hydrogel Scaffolds and Surgical Micropuncture

Zaman Ataie, Summer Horchler, Arian Jaberi, Srinivas V. Koduru, Jessica C. El-Mallah, Mingjie Sun, Sina Kheirabadi, Alexander Kedzierski, Aneesh Risbud, Angelo Roncalli Alves E Silva, Dino J. Ravnic,* and Amir Sheikhi*

Bulk hydrogel scaffolds are common in reconstructive surgery. They allow for the staged repair of soft tissue loss by providing a base for revascularization. Unfortunately, they are limited by both slow and random vascularization, which may manifest as treatment failure or suboptimal repair. Rapidly inducing patterned vascularization within biomaterials has profound translational implications for current clinical treatment paradigms and the scaleup of regenerative engineering platforms. To address this long-standing challenge, a novel microsurgical approach and granular hydrogel scaffold (GHS) technology are co-developed to hasten and pattern microvascular network formation. In surgical micropuncture (MP), targeted recipient blood vessels are perforated using a microneedle to accelerate cell extravasation and angiogenic outgrowth. By combining MP with an adjacent GHS with precisely tailored void space architecture, microvascular pattern formation as assessed by density, diameter, length, and intercapillary distance is rapidly guided. This work opens new translational opportunities for microvascular engineering, advancing reconstructive surgery, and regenerative medicine.

1. Introduction

Tissue deficiencies can occur after a traumatic event or oncologic resection.[1] Patients often suffer from infection, immobility, and dysfunction,[2–4] and with severe injuries, loss of limb, and even life may occur. Over the past two decades, hydrogel-based scaffolds have become vital to tissue reconstruction by providing a base for revascularization.[5–8] Thus, surgeons have widely incorporated hydrogel-based technologies into patient care. Unfortunately, hydrogel scaffolds are still plagued by some major limitations, including slow and random vascularization.[9] Slow or inadequate vascular integration may lead to suboptimal outcomes, including seroma, infection, and reconstructive failure.[10,11] Surgeons have explored various techniques to promote angiogenesis in the wound bed, including intrinsic vascularization.[12,13] This approach enhances neovascularization by supplying host blood via methods, such as arteriovenous loops (AVL)[14] or isolated vascular pedicles.[14] Vascular pedicles which consist of arteries and veins are commonly isolated in plastic chambers and are able to form vascular networks.[15,16] When combined with different scaffold architectures, e.g., microchannels,[17] they accelerate the neovascularization.[18,19] The field of regenerative medicine has witnessed the emergence of prevascularized scaffolds as a strategy for cell-based proangiogenic therapies,[20–22] vascularized tissue flaps,[23,24] and functional organ development.[25] These

---

Z. Ataie, A. Jaberi, S. Kheirabadi, A. R. A. E Silva[+], A. Sheikhi
Department of Chemical Engineering
The Pennsylvania State University
University Park, PA 16802, USA
E-mail: sheikhi@psu.edu

S. Horchler, S. V. Koduru, J. C. El-Mallah, M. Sun, D. J. Ravnic
Division of Plastic Surgery
Department of Surgery
Penn State Health Milton S. Hershey Medical Center
Hershey, PA 17033, USA
E-mail: dur2@psu.edu

A. Kedzierski, A. Risbud, A. Sheikhi
Department of Biomedical Engineering
The Pennsylvania State University
University Park, PA 16802, USA

D. J. Ravnic
Huck Institutes of the Life Sciences
The Pennsylvania State University
University Park, PA 16802, USA

[+]Present address: Experimental Biology Center (NUBEX), University of Fortaleza (UNIFOR), Fortaleza, CE 60811, Brazil

**ADVANCED
SCIENCE NEWS**
www.advancedsciencenews.com

NANO · MICRO
small
www.small-journal.com

scaffolds integrate porous structures with endothelial cells, co-cultured with support cells,[26] and/or with human-induced pluripotent stem cell (iPSC)-derived endothelial cells or early vascular cell progenitors.[25,27–29] Cell-laden hydrogel microparticles (microgels) have also been used to mimic the complexity and functionality of engineered vascular tissues.[21,30]

We have recently developed a novel microsurgical approach termed micropuncture (MP) that significantly expedites scaffold vascularization.[31] However, the MP-induced neovasculature in bulk hydrogels is random in nature, which does not fulfill the requirements of reconstructive surgeons where form dictates function.[32] It is well known that the structural characteristics of scaffolds profoundly affect cell infiltration and vascular ingrowth.[33] We[34,35] and others[36,37] have realized that bulk hydrogels do not allow immediate cell infiltration, hence vascularization, because they lack interconnected pores, have nanoscale pores that are about three orders of magnitude smaller than cell size, and require degradation and remodeling that may take weeks, if not months. These shortcomings impede bulk hydrogel scaffolds from undergoing optimally swift and patterned vascularization.

Architecturally, microengineered void spaces in hydrogel scaffolds are a cue for neovascularization.[38] Interconnected pores enhance cell migration and proliferation, perfusability, and nutrient/oxygen transfer, which are all pivotal factors in vascularization and tissue growth.[39] By tuning pore characteristics, such as size, interconnectivity, distribution, shape/architecture, and surface topography, properties of vascular networks may be regulated.[39] Different types of biomaterials, such as polyethylene glycol (PEG),[40] gelatin,[41] alginate,[42] and tricalcium phosphate,[43,44] have been used for fabricating porous scaffolds using particle leaching,[40] 3D (bio)printing,[41,45,46] templating,[43,47] or freeze-drying.[42] These methods based on postprocessing, often yield random pore networks or cause non-interconnected void spaces, which may limit physiologic vascularization. Granular hydrogel scaffolds (GHS), made up of assembled microgels, enable the formation of precisely controlled, interconnected cell-scale pores. This characteristic is beneficial for tissue ingrowth, cell extravasation, vascularization, and tissue regeneration.[48,49] Thus, GHS have been explored for soft tissue regeneration, e.g., in skin wound healing,[50–52] brain tissue regeneration after stroke,[53] and cardiac tissue regeneration after myocardial infarction.[54] Although some literature has demonstrated the formation of vascularized tissue using porous scaffolds,[55] to the best of our knowledge, no efforts have been devoted to accelerating the formation of patterned vascular networks in GHS.

In this work, we aim to combine our recent advances in reconstructive microsurgery[31] and hydrogel microfabrication technology[34,35,56,57] to provide an innovative synergistic platform that enables rapid perfusability and microvasculature patterning within an implanted scaffold. We will induce surgical MP in which small perforations are created using a microscale needle in the recipient vasculature to facilitate cellular extravasation and angiogenesis without causing thrombosis or significant hemorrhage, followed by guiding microvascular development using adjacent GHS with well-defined void architecture, formed via the photoassembly of microgels. We speculate that this technology may open unprecedented opportunities to redefine the tissue vascularization landscape with widespread applicability across all anatomic sites and disease etiology, including cardiovascular-related pathologies, the leading cause of morbidity and mortality worldwide.[58]

2. Results and Discussion

To form GHS building blocks, monodispersed droplets of a gelatin methacryloyl (GelMA) solution (10 wt%) were fabricated as a dispersed phase in a continuous oil phase using a high-throughput step-emulsification microfluidic device,[35,59] followed by microgel formation via physical (thermal) crosslinking at 4 °C, as shown in **Figure 1**A. The physical crosslinking stabilizes the microgels, enabling oil and surfactant removal and microgel transfer to aqueous media. Stabilized microgels were packed in an aqueous medium via centrifugation, and intraparticle crosslinking and interparticle covalent bonding were established via the photoinduced free radical polymerization of GelMA vinyl groups, yielding the GHS. GelMA is a widely used biomaterial for engineering vascular networks as it bears a plenitude of cell-adhesive moieties, such as the arginylglycylaspartic acid (RGD) peptide motif, providing design flexibility to support endothelial cell adhesion and vessel formation.[60–63] Gelatin-based hydrogels have commonly been used as protein-based biomaterials for microvasculature formation[62,64] alongside collagen and fibrin,[62] which permit network formation in micropatterned architectures[65–67] or bioprinted constructs.[66,67]

In the step-emulsification microfluidic devices, droplet size is regulated by the channel height.[68] Devices with a step size of ≈8, ≈27, or ≈60 μm were fabricated to generate a range of droplet sizes, as shown in Figure 1B. Figure 1C presents the size frequency histogram of small, medium, or large droplets, which have an average diameter of 29 ± 3 (small), 81 ± 4 (medium), or 173 ± 11 μm (large), respectively. These microgel sizes are designed to impart the GHS with a median pore diameter comparable with the size of mammalian cells, such as the stromal vascular fraction (SVF) of adipose tissue, including endothelial progenitors and immune cells that play key roles in vascular network formation.[69]

GHS may readily be used in combination with our established microsurgical approach, i.e., MP, in which blood vessels are punctured with an ultrafine microneedle to create perforations in the wall of a target recipient vessel.[31] MP promotes rapid cell extravasation and accelerates adjacent microvasculature network formation.[31] In this procedure, schematically shown in Figure 1D, the hindlimb femoral artery and vein undergo MP, followed by the implantation of GHS on the vessels. Figure 1E shows the schematic illustration of GHS with small (GHS-S), medium (GHS-M), and large (GHS-L) microgel building blocks, alongside a bulk hydrogel scaffold, placed on the vein and artery after MP. We hypothesize that the vascular microarchitecture may be guided by GHS pore characteristics.

Figure 2 presents the pore features and mechanical properties of GHS, fabricated using varying sizes of microgels. High-molecular-weight fluorescent dextran polymers (≈2 MDa, equivalent Stokes diameter ≈ 54 nm)[70] did not penetrate the microgels, labeling the interstitial void spaces of GHS. Figure 2A and Videos S1–S3 (Supporting Information) show the Z-stacked and 3D fluorescence images of porous GHS. Void fraction and
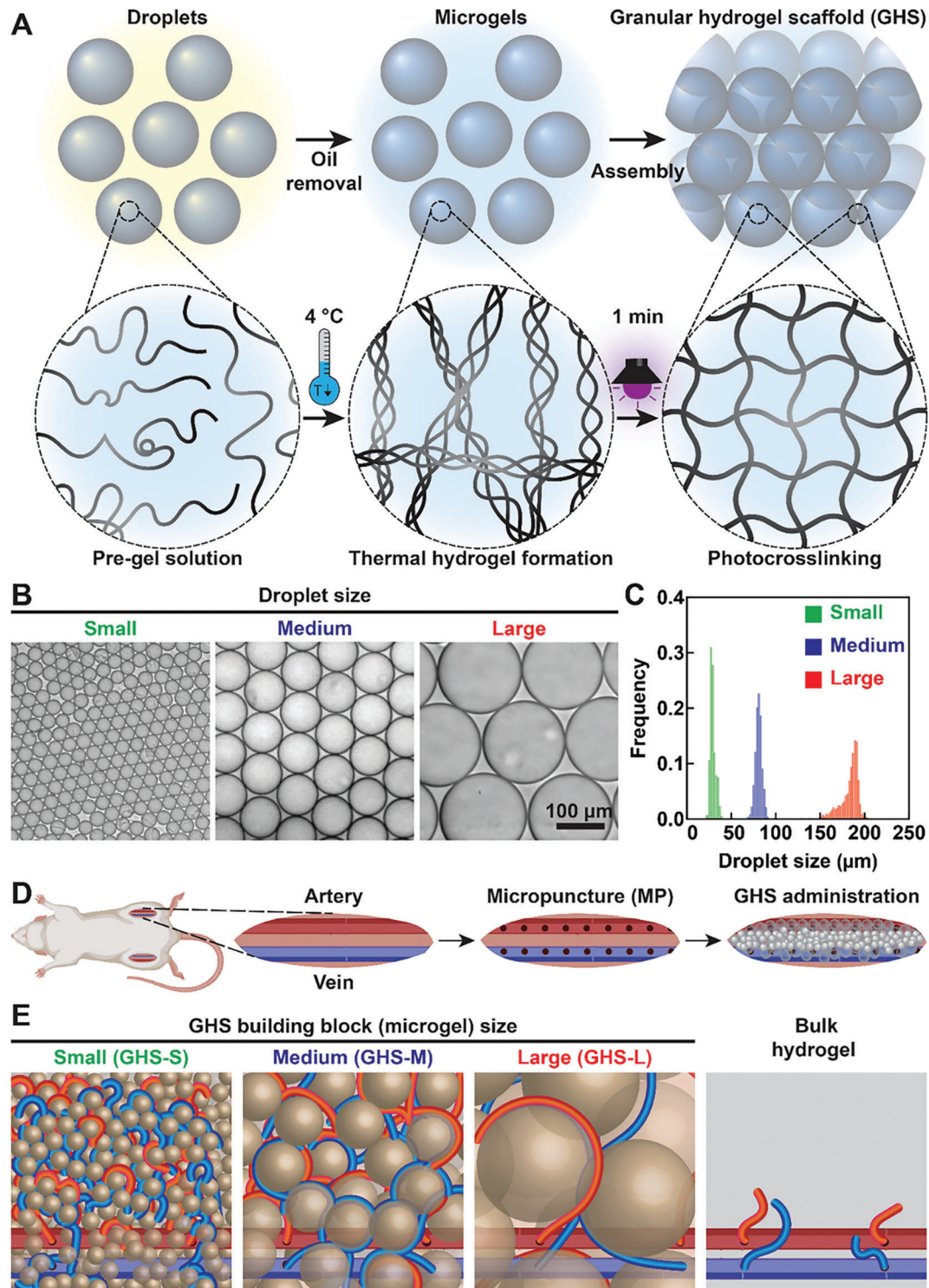
ADVANCED
SCIENCE NEWS
www.advancedsciencenews.com

NANO · MICRO
small
www.small-journal.com

Figure 1. Fabrication of GelMA microgels and GHS formation combined with MP to accelerate and guide vascular microarchitecture. A) GelMA droplets are converted to microgels via physical crosslinking at 4 °C, followed by packing and chemical assembly via photocrosslinking to yield GHS. B) Optical Microscopy images of small, medium, and large GelMA droplets. C) Droplet size frequency histogram based on $n > 2000$ droplets, indicating monodispersed droplet formation with an average diameter of ≈29 µm (small), ≈81 µm (medium), or ≈173 µm (large). D) To hasten vascularization, MP is performed on arteries and veins using a 60 µm microneedle at ≈1 mm intervals, followed by the implantation of GHS adjacent to MP vessels to guide vascular network architecture. E) Small, medium, or large microgel building blocks yield GHS with varying pore microarchitectures that guide the scattering, diameter, and length of blood vessels. The hybrid GHS and MP will therefore hasten and guide vascularization synergistically.
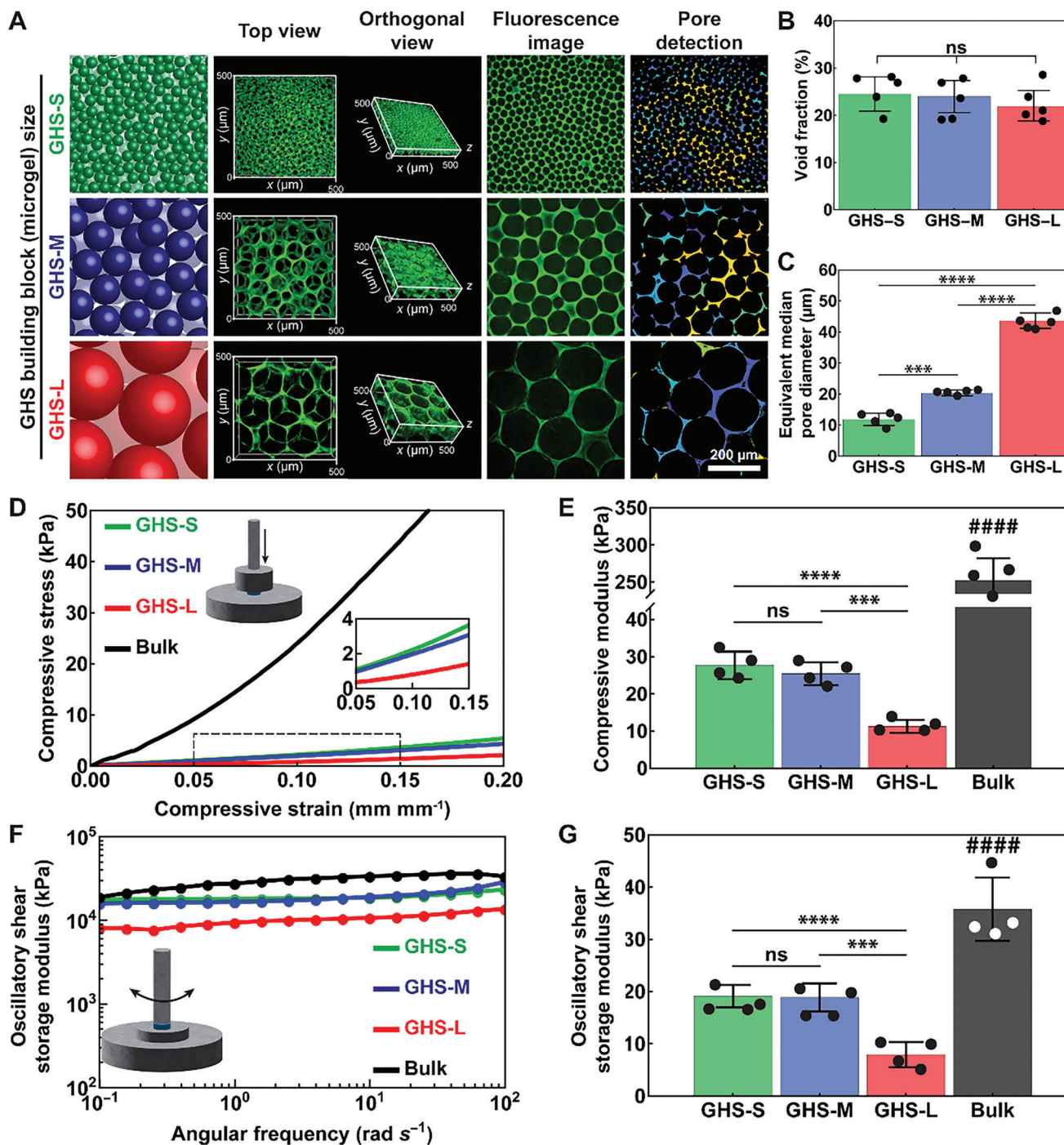
Figure 2. Microarchitecture and mechanical/rheological properties of GHS. A) The assembly of small, medium, or large microgels yields GHS with tailored pore features, imaged at varying heights (Z-stacks) and in 3D. The pores were detected using a high-molecular-weight fluorescent dye (average molecular weight ≈2 MDa), followed by analyzing fluorescence slices using a MATLAB code for pore detection. B) Effect of microgel size on GHS void fraction, defined as the volume ratio of interstitial void spaces to the total scaffold volume, showing that the void fraction is independent of the spherical building blocks ($n = 5$). C) Equivalent median pore diameter, as an indicator of GHS pore size, increases by increasing microgel size ($n = 5$). D) Compressive stress–strain curves for GHS comprising of small, medium, or large microgels alongside the bulk hydrogel counterpart (GelMA concentration = 10 wt%) as a control. E) Compressive modulus is measured based on the slope of strain–stress curves in the elastic region (≈0.05–0.15 mm mm^{-1}, $n = 4$). F) Frequency sweep tests, performed on samples at $10^{-1} – 10^2$ rad s^{-1} and a constant strain of 0.1%, i.e., the linear viscoelastic region (LVR). G) The oscillatory shear storage modulus of GHS and bulk hydrogel at 1 rad s^{-1} and 0.1% of strain ($n = 4$). B,C,E,G) One-way analysis of variance (ANOVA) was performed with the Tukey's multiple comparison test. Significant differences are indicated with ***$p < 0.001$ and ****$p < 0.0001$; ns denotes nonsignificant, with $p > 0.05$. Also, #### shows $p < 0.0001$ when comparing the bulk hydrogel control with any GHS.

**ADVANCED
SCIENCE NEWS**

www.advancedsciencenews.com

**NANO · MICRO
small**

www.small-journal.com

equivalent median pore diameter were quantified via analyzing the 3D images. The volume ratio of void spaces to the total scaffold volume was reported as the void fraction in Figure 2B. Void fraction of GHS ≈ 20–25%, which was not significantly affected by varying spherical microgel sizes; however, the void spaces are enlarged by increasing the microgel size, as shown in Figure 2C. Small, medium, or large microgels yielded GHS-S, GHS-M, or GHS-L with a median equivalent pore diameter of 12 ± 2, 20 ± 2, or 44 ± 3 µm, respectively.

Figures 2D–G show the mechanical and rheological characterizations of GHS via compression and oscillatory rheology tests. Figure 2D presents the compressive stress–strain curves of GHS and the bulk hydrogel counterpart comprising similar GelMA polymer concentration. At any compressive strain, the stress value of GHS was lower than the bulk hydrogel. This is a result of the porous GHS structure and limited contact area between adjacent microgels, which has also been reported in our previous publications.[34,35] The slope of stress–strain curves at the elastic region, typically at ≈0.05–0.15 mm mm^{-1}, was calculated and reported as the compressive modulus in Figure 2E. The compressive modulus was significantly lower in GHS-L than GHS-S or GHS-M, possibly resulting from larger void space and weakened microgel–microgel contact among large microgels per unit volume. In addition, the compressive modulus of bulk hydrogel was about one order of magnitude higher than GHS, which also represents the local compressive modulus of microgels. The GHS stiffness was in the range of human soft tissues.[71,72]

Viscoelastic properties of GHS were characterized via oscillatory rheology. Samples were assessed based on the oscillatory strain sweep ranging from 10^{-2} to 10^2% at a constant angular frequency of 1 rad s^{-1} to determine the linear viscoelastic region (LVR) and flow point (Figure S1, Supporting Information). As the LVR for all the gels was below ≈1% of strain at 1 rad s^{-1}, the oscillatory frequency sweep was performed at 10^{-1}–10^2 rad s^{-1} and at a constant strain of 0.1% (Figure 2F). The oscillatory shear storage modulus for GHS-L was lower than GHS-S or GHS-M, and the storage modulus of bulk hydrogel was higher than all GHS, as presented in Figure 2G. Overall, the storage modulus had a similar trend as the compressive modulus.

To examine the effect of scaffold microarchitecture on in vitro cell activity, GHS with tailored microscale pores were seeded with human SVF cells and compared with the bulk hydrogel counterpart (nanoporous, GelMA concentration = 10 wt%), as schematically presented in **Figure 3**A. The time-dependent behavior of SVF cells cultured in microvascular endothelial growth media[73] is shown in Figure 3B. While the cells remained nonprolific, round-shaped, and incapable of network formation in the bulk GelMA hydrogel, they were able to readily spread in GHS. Among GHS, GHS-L was not able to maintain all the SVF cells among the microgels because the pores were too large compared with the cell size. Figure S2 (Supporting Information) shows that within 90 min of seeding, GHS-S and GHS-M hold almost all the cells, whereas the majority of cells are entrained out of GHS-L.

Figure 3C presents the roundness of cells in the scaffolds, showing that encapsulated cells in the bulk hydrogel had significantly higher roundness (0.86 ± 0.02) compared with the elongated cells in GHS (GHS-S ≈ 0.54 ± 0.04, GHS-M ≈ 0.45 ± 0.01, GHS-L ≈ 0.54 ± 0.05). Importantly, cells started forming networks in GHS-S and GHS-M within 2 days; however, no network

was observed in GHS-L. Figures 3D,E present the projected cell area and the number of network branches, respectively. Unlike the bulk hydrogel, the porous structure of GHS-S and GHS-M facilitated network formation via increasing cell coverage (projected area) and number of branches. The ability to form such networks is essential for successful in vivo vascularization. When the median pore size was significantly larger than cell size, i.e., in GHS-L, cells were not able to form any network, and cell–cell connections were weakened. Initial cell seeding density affected the network formation quality in GHS, as presented in Figure S3 (Supporting Information), which is also reported for bulk hydrogels.[74] At an exceeding low or high seeding density, the cells were not able to form any network in the GHS, because of the lack of cell–cell connection or becoming overconfluent, respectively. Figure S4 (Supporting Information) presents the effect of SVF cell seeding density on network formation capability in the bulk GelMA hydrogel. Independent of cell seeding density, the bulk GelMA hydrogel (10 wt%) was unable to support network formation because of impaired cell spreading. These data shed light on why currently used bulk scaffolds in clinical settings are unable to provide an optimal vascularization platform. Accordingly, there exists an optimal pore size range in GHS that promotes cell network formation and, consequently, vascularization, which will further be investigated in vivo.

GHS or bulk hydrogel scaffolds were implanted adjacent to the MP artery and vein. Figure S5 (Supporting Information) shows a gross image of an implanted scaffold after MP microsurgery. Implanted scaffolds in MP and non-MP (control) groups were analyzed at day 7 to assess in vivo cellular infiltration and neovascular network formation, as presented in **Figure 4**. GHS placed adjacent to the MP artery and vein underwent an increase in cellular infiltration independent of microgel size. On the other hand, no significant cellular infiltration was observed in the implanted bulk hydrogels because of its nanoporous structure. MP allowed for rapid cellular extravasation into GHS, and GHS enabled accelerated inward cell infiltration. An increased accumulation of endothelial cells was observed in the lining of MP scaffold pores, along with the formation of new microvascular capillary networks around the microgels (Figure 4A).

Accelerated neovascularization was patterned by using different sizes of microgel building blocks. Varying the GHS pore size caused differences in the accessible space for neovascular plexus formation originating from the adjacent femoral artery and vein. Using artificial intelligence (AI), the fluorescence images were analyzed and quantified (Figure S6, Supporting Information). Figure 4B presents the mean vascular density of GHS and bulk scaffolds implanted adjacent to MP or non-MP (control) vessels after 7 days. With MP, the vascular density of GHS-M and GHS-S was significantly higher than GHS-L and bulk. Results showed the significance of MP in neovascularization, especially in GHS-S and GHS-M. GHS-L did not show any significant difference with MP versus without MP, possibly due to the extra-large void spaces, which bypass the vessel formation capacity. Results show that the mean vascular density is significantly impacted by the synergistic interactions between pore features and MP (Table S1, Supporting Information). No significant vascular ingrowth was obtained in the adjacent bulk GelMA scaffold, and the results could not be analyzed due to vessel scarcity. Under these conditions it appeared that even though MP provided a rapid route
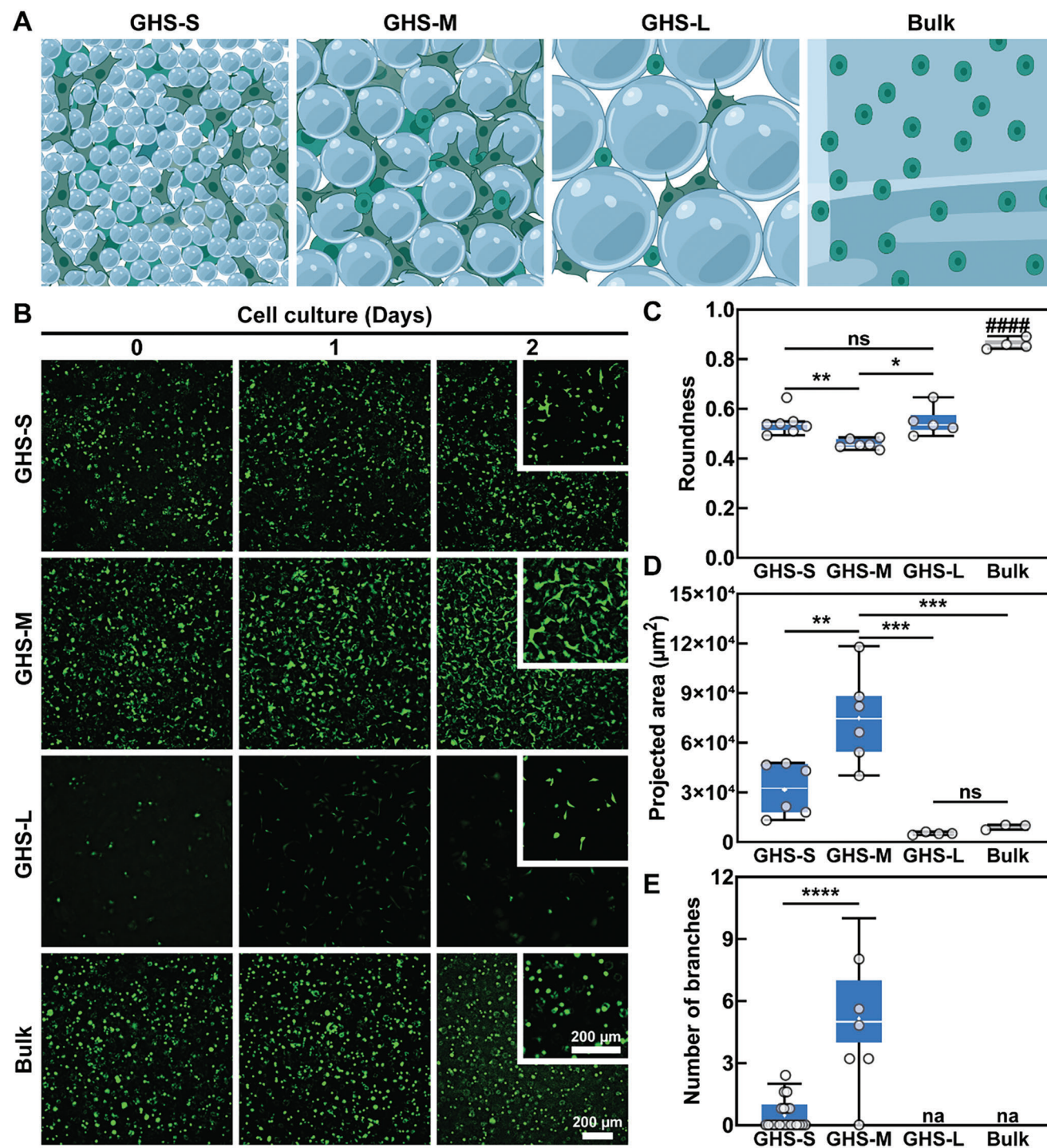
**ADVANCED
SCIENCE NEWS**

www.advancedsciencenews.com

NANO · MICRO

small

www.small-journal.com

Figure 3. Scaffold microarchitecture regulates human SVF cell behavior and network formation. A) Schematic of cells seeded in porous GHS assembled using varying GelMA microgel sizes compared with a bulk, nanoporous GelMA hydrogel scaffold. B) GHS-S and more significantly GHS-M promote SVF network formation, whereas GHS-L does not yield any network. The bulk GelMA hydrogel scaffold does not support SVF cell proliferation and 3D network formation. C) Roundness of encapsulated SVF cells in GHS or bulk scaffolds, which is ≈40–60% or 90%, respectively. SVF cells elongate more in GHS-M compared with GHS-S and GHS-L, and do not elongate in the bulk scaffold at all. D) Total projected area of SVF cells, which was significantly higher in GHS-M compared with GHS-L and bulk GelMA. E) Number of SVF cell network branches in the scaffolds, showing excellent branch formation in GHS-M, some branch formation in GHS-S, and no branches in GHS-L or bulk scaffold after 2 days of culture. In panels (C) and (D), one-way ANOVA was performed with the Tukey's multiple comparison test. In panel (E), unpaired two-tailed t-test was done. Significant differences are indicated with $*p < 0.05$, $**p < 0.01$, $***p < 0.001$, and $****p < 0.0001$; na denotes nonapplicable, ns denotes non-significant, with $p > 0.05$. In panel (C), #### shows $p < 0.0001$ when comparing the bulk hydrogel control with the GHS groups. Number of scaffolds per group was at least 3. The region of interest was $1330 \times 1330 \ \mu m^2$.

**ADVANCED
SCIENCE NEWS**

www.advancedsciencenews.com
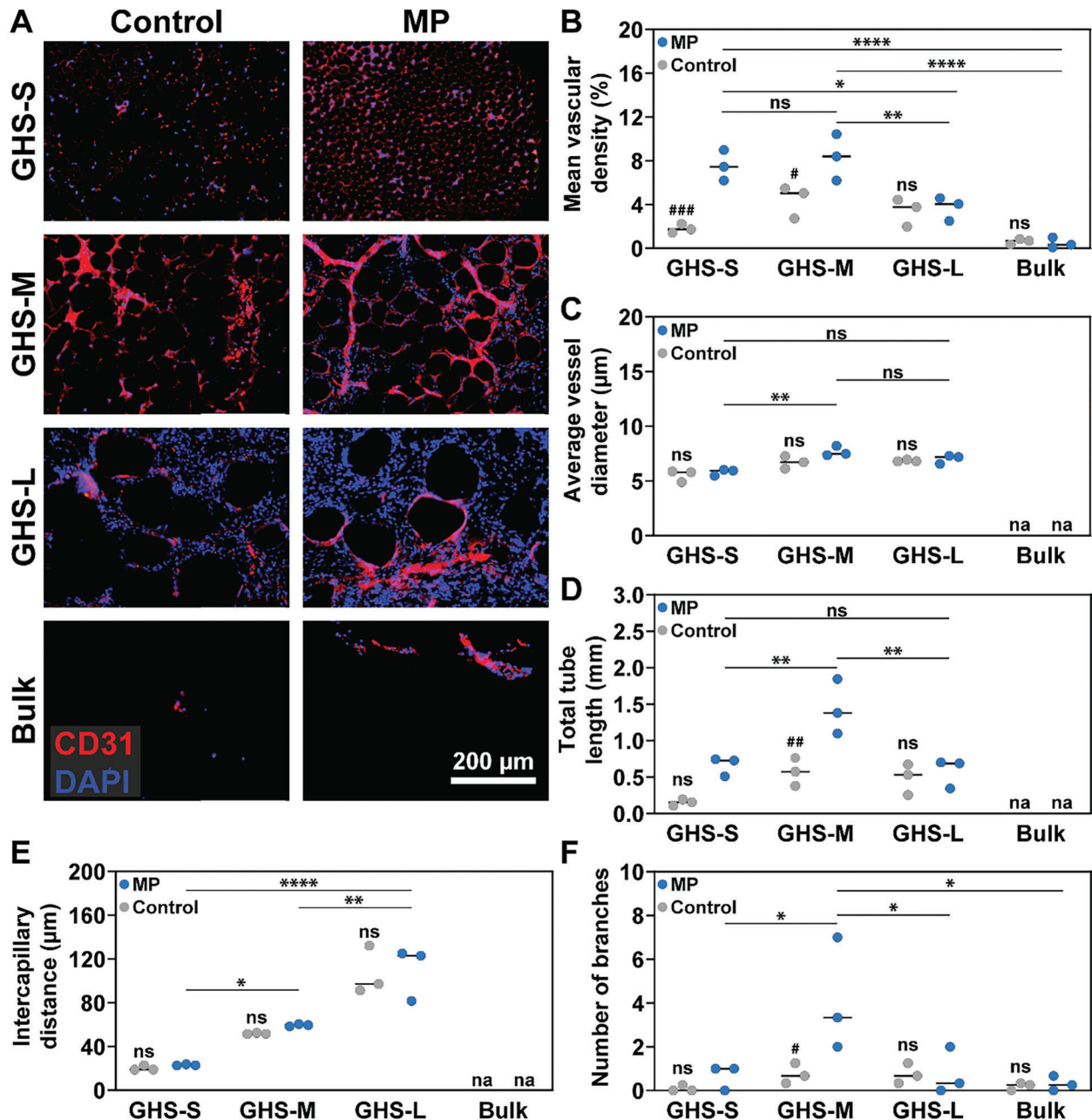
NANO · MICRO

small

www.small-journal.com

Figure 4. Hybrid MP and GHS hasten and pattern in vivo vascularization. A) After explanation, scaffolds were stained against CD31(red) to demonstrate endothelial cells. A 4′,6-diamidino-2-phenylindole (DAPI) counterstain (blue) was used to delineate all nucleated cells. GHS without MP (control) enabled some vascular formation. Synergizing GHS with MP resulted in significantly higher endothelial cell infiltration and vascularization across microgel sizes. The bulk GelMA hydrogel scaffold either without MP (control) or with MP underwent limited vascular formation. B–F) AI quantification of scaffold vasculature (CD31). Bulk scaffolds (control) could not be analyzed for diameter, length, and intercapillary distance because of vessel scarcity. B) Mean vascular density in the scaffolds, showing enhanced network formation in GHS-S and GHS-M with MP. MP did not result in any significant difference in neovascularization using GHS-L or bulk hydrogel. C) The average vessel diameter of vascular networks formed in varying scaffolds, showing almost similar values for all the GHS groups. D) Total tube length in varying scaffolds, showing that GHS-M with MP promoted the formation of longest tubes. GHS-S and GHS-L yielded significantly lower tube length than MP GHS-M. E) Intercapillary distance in varying scaffolds, which are correlated directly with microgel size: the larger the microgels, the higher the intercapillary distances in GHS. F) Number of branches in varying scaffolds, showing that MP GHS-M yields a significantly higher number of branches than any other study group. Two-way ANOVA was performed with the Holm–Šídák's multiple comparison test, and significant differences are indicated with $*p < 0.05$, $**p < 0.01$, and $****p < 0.0001$. Note na implies nonapplicable, and ns indicates nonsignificant ($p > 0.05$). When comparing the control (non-MP) with MP of each group, ns indicates nonsignificant with $p > 0.05$, and the level of significance is shown with $\#p < 0.05$, $\#\#p < 0.01$, and $\#\#\#p < 0.001$ above the control group. Number of animals per group was 3. Each data point in panels (B–F) shows the average of at least three images taken from each hindlimb (region of interest = 580.50 × 435.37 μm^2), analyzed using the AI.

ADVANCED
SCIENCE NEWS
www.advancedsciencenews.com

NANO · MICRO
small
www.small-journal.com

of cellular extravasation from the targeted vasculature, the bulk hydrogel scaffold characteristics were insufficient to support cell infiltration. Increased endothelial cell infiltration (Figure 4A) appeared concordant with the vascular density observed in MP GHS.

Figure 4C presents average vessel diameter, which was in the range of 5–10 μm among the GHS groups. Statistical analyses show that the size of newly formed vessels is not MP dependent. Additionally, void space size did not significantly affect the vessel diameter, except for GHS-M which yielded slightly larger vessels compared with GHS-S (Table S2, Supporting Information). Figure 4D shows that the tube length was significantly higher in MP GHS-M due to the significant expansion of small branching outgrowths and neovessel formation. MP and void space size significantly affected total scaffold tube length (Table S3, Supporting Information). As presented in Figure 4E and Table S4 (Supporting Information), intercapillary distance was a function of spacing, dictated by GHS building block size, which was independent of MP. This shows that the vascular network can readily be patterned by GHS microarchitecture in vivo. The total number of branches in the field of view is shown in Figure 4F, indicating significantly pronounced neovascular network formation using MP GHS-M. All other groups, including non-MP (control) groups (Table S5, Supporting Information) did not yield significant branch numbers as a result of either extremely small or large pores.

It has been demonstrated that macrophages are integral to angiogenesis.[75–77] To understand their correlation to enhanced GHS vascularization after MP, scaffold macrophages were stained against F4/80 (green) and 4′,6-diamidino-2-phenylindole (DAPI, blue) at day 7, as shown in **Figure 5**A. It was observed that vascularization in the GHS corresponded to early macrophage accumulation. Figure 5B presents the area correlated to the stained macrophages across conditions (*p*-values may be found in Table S6 in the Supporting Information). The highest extent of scaffold macrophage infiltration was observed in GHS-M, which is consistent with the highest vascular density, total tube length, and the number of branches yielded in this scaffold. Accordingly, the optimum median pore size of GHS to maximize the quality of neovascularization is about 20 μm, a size that is comparable with the size of macrophages (10–20 μm) and endothelial cells (10–30 μm).[78,79] Previous research has shown that GHS comprising varying microgel sizes influence cell infiltration and macrophage polarization.[80,81] GHS made up of ≈48 or ≈146 μm microgels resulted in higher M1 polarization or M2 polarization in macrophages, respectively.[79] The inflammatory response of macrophages has also been shown to decrease when the GHS pore size is within the same range of cell size.[80] GHS with a similar pore size to our GHS-M (average microgel diameter ≈ 70–80 μm) had a significantly higher infiltrated cell area after 21 days of subcutaneous implantation compared with GHS made up of smaller (≈40 μm) or larger (≈130 μm) microgels.[81]

Furthermore, the cytotoxicity of scaffolds was assessed clinically via weight, and there was no associated weight loss in any animal cohort. Histology was used to demonstrate end organ normalcy, as shown in Figure 5C. No parenchymal injury was observed on liver, kidney, and spleen histology. No animals needed to be withdrawn from the study. Accordingly, GHS did not have any toxic side effects after the implantation, which is a key re-

quirement for further translational considerations. Scaffold perfusability was assessed using trichrome-stained samples to quantify cell-lined luminal structures with evidence of red blood cell (RBC) perfusion, relative to the total number of cell-lined luminal structures (Figure S7, Supporting Information). The evaluation of RBC-perfused lumens was conducted for both MP and non-MP conditions implanted with GHS-M at day 7. MP scaffolds had significantly higher perfusability in vivo.[82]

Figure 6 presents the in vivo perfusability of neovascularized implanted GHS on Day 7, which indicates that the formed vasculature is functional, interconnected, and guided by the microarchitecture of GHS pores. The in vivo perfusion assessment was conducted using implanted GHS-M (MP and non-MP control) as shown schematically in Figure 6A based on a fluorescence vessel painting technique[82] (angiogram, Figure 6B). The AI quantification showed that the MP group yielded significantly more functional and perfusable vessels compared with the non-MP control group. The MP group had significantly higher vascular density compared with the non-MP group, indicating an overall increase in neovascularization using MP (Figure 6C). The average vessel diameter was also higher, at around 20 μm, which is comparable to the median pore diameter of the implanted scaffold (Figure 6D). Moreover, the total tube length was significantly higher in the MP group, reaching as high as ≈8 mm (Figure 6E). The number of branches was also higher in the MP group, with a *p*-value of 0.0524 (Figure 6F). These findings suggest that the combination of MP and GHS accelerates the formation of functional and perfusable vessels.

3. Conclusions

Limited vascularization is a major bottleneck in reconstructive surgery and regenerative engineering. The clinical relevance of GHS lies in their ability to address the limitations of random vascularization observed in conventional bulk hydrogel scaffolds. While random vascularization may be sufficient for simple tissue reconstruction, it hinders advanced tissue regeneration, where the establishment of a precise microvascular infrastructure is crucial for achieving both form and function. The lack of appropriate cues to guide the spatiotemporal coordination of vessel growth, remodeling, maturation, and stabilization leads to aberrant angiogenesis and pathological vessel formation that persists even after vascular perfusion is established.[83] This presents a significant challenge for surgeons aiming to replace lost tissue with functional tissue. GHS offer a potential solution to this bottleneck, as their microengineered structure allows for the creation of precisely controlled and interconnected void spaces that guide neovascularization for soft tissue engineering and regeneration.

In this study, we proposed a hybrid technology using a novel microsurgical approach (MP) and porous GHS. GHS was engineered using three different sizes of microgel building blocks to precisely tailor scaffold microarchitecture, which was used to pattern microvascular networks in rat hindlimbs. MP was used as a facile microsurgical approach to rapidly vascularize adjacent GHS within 7 days. Accelerated and guided vascularization were correlated to early macrophage and endothelial cell accumulation within MP scaffolds, showing that GHS provide a suitable base for neovascularization. Importantly, the optimum
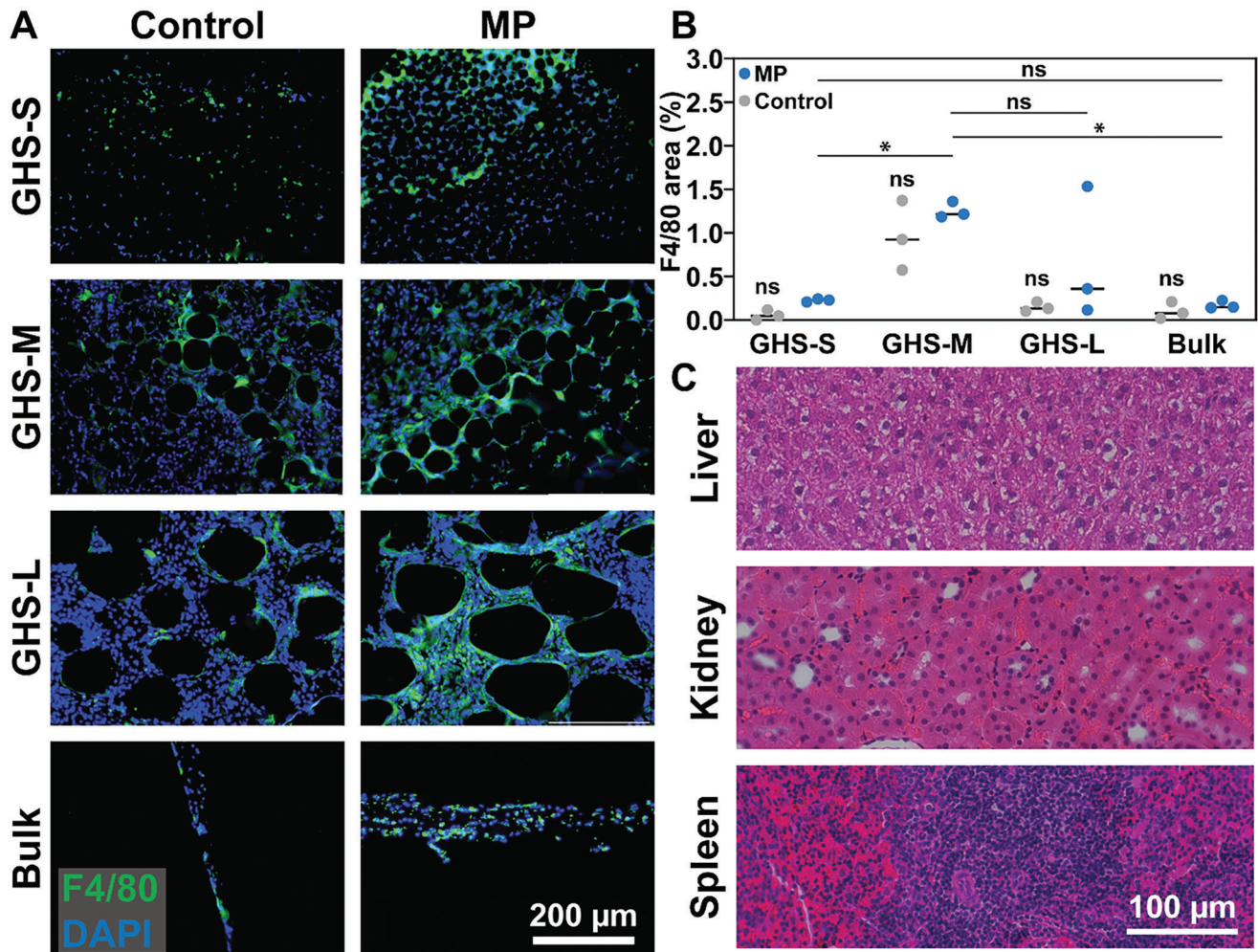
ADVANCED
SCIENCE NEWS
www.advancedsciencenews.com

NANO · MICRO
small
www.small-journal.com

Figure 5. Macrophage accumulation in GHS and cytotoxicity assessments. A) Following scaffold explanation and staining with F4/80 (green) and DAPI (blue), MP GHS had a larger proportion of infiltrating macrophages across all microgel sizes compared with non-MP GHS. Some macrophage infiltration was seen in GHS without MP (control). Bulk GelMA either without MP (control) or with MP failed to enable significant macrophage accumulation. B) The area of F4/80-stained cells, quantifying the extent of macrophage accumulation in the scaffolds. MP GHS explants underwent an increase in macrophage accumulation. Bulk hydrogels did not permit significant macrophage infiltration. C) Histological assessment of systemic toxicity in liver, kidney, and spleen after 7 days of GHS-M implantation. GHS-M had no adverse effects either clinically or histologically, following a 1 week implantation period in rats. The two-way ANOVA was performed with the Holm–Šídák's multiple comparison test, and significant differences are indicated with $*p < 0.05$. Here, ns (nonsignificant) is $p > 0.05$. When comparing the control (non-MP) with MP of each group, nonsignificancy with $p > 0.05$ was shown by ns above the control group. Number of animals per group was 3. Each data point in panel (B) shows the average of at least three images taken from each hindlimb (region of interest = $580.50 \times 435.37\ \mu m^2$), analyzed using the AI.

scaffold microarchitecture was identified in GHS-M, which had interconnected cell-scale pore characteristics that significantly promoted vascular network formation in terms of mean vascular density, average vessel diameter, and total tube length. In addition, the microvasculature was patterned at varying intercapillary distances using GHS with varying microgel building block sizes, and no systemic cytotoxicity was identified. Lastly and most importantly, the induced microvasculature was highly perfusable, representing a significant advancement in tissue engineering prior to clinical translation. We anticipate that the hybrid MP–GHS technology provides unique opportunities for physiologic neovascularization and sets up a novel translational platform for reconstructive surgery and regenerative engineering.

4. Experimental Section

Materials: Gelatin type A from porcine skin (≈300 g Bloom), methacrylic anhydride (containing 2000 ppm topanol A as an inhibitor, 94% purity), Dulbecco's phosphate-buffered saline (DPBS), lithium phenyl-2,4,6-trimethylbenzoylphosphinate (LAP), trichloro(1*H*,1*H*,2*H*,2*H*-perfluorooctyl)silane (F-silane), fluorescein isothiocyanate–dextran (FITC–dextran) with an average molecular weight of 2 MDa, hematoxylin and eosin (H&E) staining kit, xylenes (mixed isomers, histological grade), D-(+)-glucose (1 M, sterile-filtered), glutaraldehyde solution (grade II, 25 vol% in H_2O), and 1,1-dioctadecyl-3,3,3,3-tetramethylindocarbocyanine perchlorate (carbocyanine) were purchased from Sigma, MA, USA. Glass slides, vacuum filtration (pore size = 0.20 μm) systems, and formalin solution (10 wt% neutral buffered) were purchased from VWR, PA, USA, and silicon wafers (4 in.) were

ADVANCED
SCIENCE NEWS

www.advancedsciencenews.com

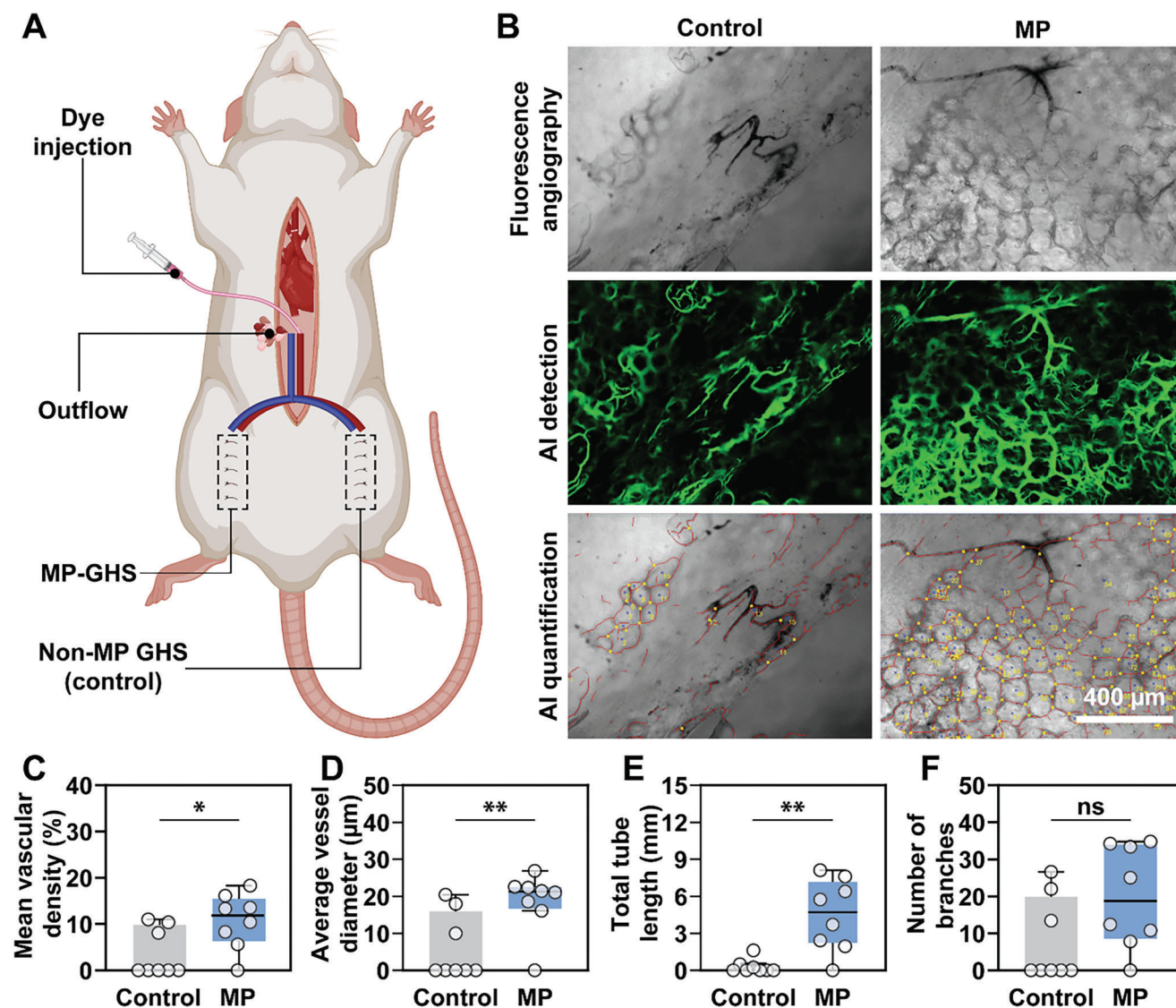NANO · MICRO
small
www.small-journal.com

Figure 6. In vivo perfusion assessment and quantification of vascularized GHS-M at day 7. A) Schematic illustration of perfusion assessment procedure, showing the perfusion of GHS-M with and without MP. B) Fluorescence images were acquired from each group (MP and the non-MP control) and quantified using the AI. Both raw and analyzed images showed significantly more perfusable vasculature formation in MP-GHS at day 7. C–F) Quantification of C) vascular density, D) vessel diameter, E) total tube length, and F) number of branches for implanted GHS-M with MP or without MP (control) at day 7. Paired two-tailed t-tests were performed, and significant differences are indicated with $*p = 0.0130$ (panel C), $**p = 0.0061$ (panel D), $**p = 0.0052$ (panel E), and ns with $p = 0.0524$ (panel F). Number of animals per group was 8. Each data point in panels (C)–(F) shows the average of five images taken from each hindlimb (region of interest = $1161.00 \times 870.75 \ \mu m^2$), analyzed using the AI.

procured from University Wafers, MA, USA. Negative photoresists were all from the KMPR 1000 series, Kayaku Advanced Materials, MA, USA. The polydimethylsiloxane (PDMS) SYLGARD 184 kit was purchased from Dow Corning, MI, USA. Ultrapure Milli-Q water with an electrical resistivity of $\approx 18 \ M\Omega$ at 25 °C was provided by a purification system, manufactured by the Millipore Corporation, MA, USA. Dialysis membranes with 12–14 kDa molecular weight cutoff were purchased from Spectrum Laboratories, NJ, USA. Novec 7500 Engineered Fluid (Novec oil) was provided by 3 M, MN, USA. Pico-Surf (5 vol% in Novec) was purchased from Cambridge, UK, and $1H,1H,2H,2H$-perfluoro-1-octanol (PFO) was supplied by Alfa Aeser, MA, USA. Mesenchymal stem cell growth medium 2 and endothelial cell growth medium MV (low-serum cell culture medium for endothelial cells from microvascular vessels, the coronary artery, and the aorta) were

purchased from PromoCell, Germany. Hanks' balanced salt solution (HBSS) and phosphate-buffered saline (PBS, 1X, without Ca, Mg, phenol red, 0.1 μm sterile filtered) were obtained from Genesee Scientific, CA, USA. CellTracker green 5-chloromethylfluorescein diacetate (CMFDA), 100 and 40 μm strainers, collagenase type I, and RBC lysis buffer were procured from ThermoFisher, MA, USA. Ethanol (absolute, anhydrous, 200 proof) was purchased from Greenfield Global, CT, USA, and isoflurane was provided by Piramel, PA, USA. Mouse platelet–endothelial cell adhesion molecule (PECAM-1/CD31) antibody, a betadine-antiseptic povidone–iodine solution, was obtained from Purdue Products, CT, USA. Alexa Fluor 493 and 647 and Fluoroshield were purchased from enQuire BioReagent, CO, USA. Ficoll-Paque was acquired from GE HealthCare, PA, USA. The primary antibodies used in this study included

ADVANCED
SCIENCE NEWS

www.advancedsciencenews.com

NANO · MICRO

small

www.small-journal.com

i) Polyclonal Goat Immunoglobulin G (IgG) CD31/PECAM-1 antibody, antimouse/rat from R&D systems, and ii) Polyclonal Rabbit IgG EMR1 antibody, human, mouse, antihuman/mouse/rat from ThermoFisher. The following secondary antibodies were used: i) Polyclonal donkey IgG (H+L) highly cross-adsorbed secondary antibody, anti-goat, Alexa Fluor Plus 594 from ThermoFisher, and ii) Polyclonal donkey IgG (H+L) highly cross-adsorbed secondary antibody antirabbit, Alexa Fluor Plus 594 also from ThermoFisher.

Methods—Microfluidic Device Fabrication: Fabrication of high-throughput step emulsification was conducted via soft lithography according to the literature.[35,59] Briefly, two- or three-layered master molds were fabricated on silicon wafers using the KMPR 1000 series as the negative photoresists. The first layer was fabricated with KMPR 1005, KMPR 1025, or KMPR 1035 for small, medium, or large droplet fabrication, respectively. The spin coating condition for each mold was adopted from the manufacturer's specification sheet.[84] The first layer height was around 8, 27, or 60 µm for small, medium, or large droplet fabrication, respectively. The second layer was deposited using the KMPR 1035 to become 2–3 times larger than the anticipated droplet size, providing enough space for forming and moving droplets. The microfluidic devices were molded using the PDMS kit. The base and crosslinker of PDMS were mixed at a 10:1 mass ratio, poured onto the masters, and vacuum degassed to eliminate air bubbles, followed by curing at 80 °C for 2 h. The PDMS devices were then bonded onto precleaned glass slides via air plasma treatment at 400 mTorr for 45 s, followed by F-silane (2 vol% in Novec oil) treatment to render the devices fluorophobic. Treated devices were rinsed twice with Novec oil and maintained at 80 °C for 30 min to evaporate the remaining oil.

Methods—GelMA Polymer Synthesis: GelMA polymer was synthesized according to the previous publications.[35,56] Briefly, 20 g of gelatin Type A was added to 200 mL of DPBS at 50 °C while stirring at 200 rpm. Once gelatin was fully dissolved, the reaction was initiated by adding 16 mL of methacrylic anhydride to the solution at 50 °C. The solution was protected from light by wrapping the reaction container with aluminum foil. After 2 h, the reaction was stopped by adding 400 mL of DPBS. The diluted solution was then dialyzed against Milli-Q water at 40 °C for 10 days using the dialysis membranes (molecular weight cutoff = 12–14 kDa). Finally, the purified solution was sterile filtered using the vacuum filtration system and maintained at −80 °C for 24 h. The frozen solution was lyophilized to yield solid GelMA. The degree of substitution was 71 ± 3% (n = 3), calculated based on the published protocol.[85]

Methods—Microgel Fabrication: A GelMA polymer solution (10 wt% in DPBS) was converted to small (diameter ≈ 29 ± 3 µm), medium (≈81 ± 4 µm), or large (≈173 ± 11 µm) droplets via injecting the aqueous phase in a continuous oil phase using the step-emulsification microfluidic devices, comprising a step size of 8, 27, or 60 µm, respectively. To prepare the aqueous phase, the photoinitiator solution containing 0.1 wt% of LAP in DPBS was prepared, followed by dissolving GelMA at 50 °C to obtain a 10 wt% aqueous GelMA solution. The oil phase was Novec oil, supplemented with varying concentrations of the Pico-Surf surfactant. The concentration of surfactant in the oil was 2 vol% for the fabrication of small and medium droplets, and 0.5 vol% for the large droplets. To avoid blockage of microfluidic channels, the droplet fabrication setup was maintained at ≈40 °C using a space heater and/or a hair dryer. The fabricated droplets were shielded from light and maintained at 4 °C overnight to form physically crosslinked GelMA microgels.

Methods—GHS Fabrication: The oil and surfactant were removed from the physically crosslinked GelMA microgels via adding a solution of PFO (20 vol% in Novec oil) at a 1:1 volume ratio. The suspension was then vortexed and centrifuged at 300 × g for 15 s, followed by discarding the excess oil and surfactant and adding the photoinitiator solution (0.1 wt% in DPBS) at a 1:1 volume ratio. This mixture was again vortexed, centrifuged at 300 × g for 15 s, and separated from any remaining oil and surfactant. Microgels were then packed at a higher centrifugal force (3000 × g), and the excess photoinitiator solution was discarded. The packed microgel suspension was transferred to an acrylic mold mounted on a glass slide using a positive displacement pipette (Microman E M100E or Micro-

man E M1000E, Gilson, OH, USA). Packed small, medium, or large microgels were then photochemically crosslinked via light exposure (wavelength = 395–405 nm, intensity = 15 mW cm^{-2}, exposure time = 60 s) to form GHS-S, GHS-M, or GHS-L, respectively.

Methods—Bulk Hydrogel Scaffold Fabrication: Bulk GelMA hydrogel scaffolds were fabricated using a two-step crosslinking approach, similar to the GHS fabrication method to resemble the same local physicochemical properties.[35] In brief, lyophilized GelMA was dissolved at 50 °C in the photoinitiator solution (0.1 wt% of LAP in DPBS), yielding a clear solution with a final concentration of 10 wt% GelMA. The GelMA solution was then pipetted out using a pre-warmed (37 °C) pipette tip and poured into laser-cut acrylic molds. The molds were maintained in a custom-built humidity chamber, protected from light, and placed at 4 °C overnight for physical crosslinking. Molded scaffolds were exposed to light (wavelength = 395–405 nm, intensity = 15 mW cm^{-2}, exposure time = 60 s) to form bulk GelMA hydrogel scaffolds.

Methods—GHS Pore Characterization: GHS were fabricated in disk molds (diameter = 8 mm and height = 1 mm), followed by adding ≈20 µL of the FITC-dextran solution (concentration = 15 µM in DPBS) on top of them. The scaffolds were then imaged using a fluorescence microscope microscope (Leica DMi8 THUNDERED microscope, Germany) to generate 3D Z-stacked images with a total depth of 160, 110, or 60 µm for GHS-L, GHS-M, or GHS-S, respectively. The microscope built-in software (LAS X 5.0.3 Life Science Microscope Software Platform) was used to generate 3D images from the Z-stacked images and determine the void fraction based on the ratio of space occupied by the fluorescent dye to the total volume of imaged section. A custom-developed MATLAB code was used to measure the pore characteristics by detecting the void spaces and approximating the diameter of circles that would occupy the same area.

Methods—Compression Analysis of Scaffolds: GelMA GHS comprising varying sizes of microgel building blocks and bulk hydrogel scaffolds (as a control group, containing 10 wt.% of GelMA polymer) were fabricated in disk molds (diameter = 8 mm and height = 1 mm). Compression tests were performed using an Instron mechanical tester (Instron 5542, MA, USA) at a compression rate of 1 mm min^{-1}. To determine the compressive modulus, a linear regression was performed in the elastic region of compressive strain-stress curve, typically at strain ≈0.05–0.15 mm mm^{-1}. The slope of the regression line was reported as the compressive modulus.

Methods—Rheological Assessments of Scaffolds: To evaluate the viscoelastic properties of GHS and bulk hydrogels, disk scaffolds (diameter = 8 mm and height = 1 mm) were fabricated and accessed via oscillatory rheological tests. An AR-G2 rheometer (TA instrument, DE, USA) was equipped with an 8 mm diameter sandblasted top plate and a 25 mm bottom plate to sandwich the samples at 25 °C. Amplitude sweep tests were performed at strain ≈10^{-2}–10^2% and at a fixed frequency (1 rad s^{-1}) to determine the LVR for each scaffold. Frequency sweep tests were performed at a range from 10^{-1} to 10^2 rad s^{-1} and at a constant strain (0.1%).

Methods—Isolation of Human Adipose-Derived SVF Cells: Human SVF cells were obtained from discarded adipose tissue, obtained from consented patients undergoing elective lipectomy at The Pennsylvania State University (Hershey, PA) under Institutional Review Board (IRB) approval protocol (# 00004972).[86] The lipectomy tissue was cleaned using HBSS to remove blood, followed by mechanical mincing after which tissue was enzymatically digested using 1% collagenase at 37 °C on a shaker for 2 h. Collagenase-digested tissue was centrifuged for 10 min at 300 × g, and the pellet was collected. The pellet was then suspended in RBC lysis buffer to remove RBC. The pellet was further centrifuged and filtered through 100 and 40 µm strainers.[87,88] After re-suspension in HBSS, the pellet was layered on a Ficoll-Paque gradient and centrifuged for 20 min at 300 × g. The SVF cells, the white layer (middle) band, were identified and collected.

Methods—In Vitro Human SVF Cell Culture: Human SVF cells were cultured in the complete mesenchymal stem cell growth media at 37 °C with 5 vol% carbon dioxide (CO_2) gas. Media were changed every other day. The cells were cultured and maintained to reach 80% confluency and were fluorescently labeled using the CellTracker CMFDA dye according to the manufacturer protocol. Then, the cells (passage four) and microgels were mixed using the positive displacement pipette to yield 4 × 10^3 cells per µL of microgel suspension. To fabricate cell-laden bulk hydrogel scaf-

folds, the cells were suspended in a pre-gel solution, and the resulting suspension was used to fabricate the scaffold. The cell-laden GHS and bulk hydrogel controls were fabricated and cultured in the endothelial cell growth medium MV for 2 days. After 2 days, cells were imaged using a fluorescence microscope (Leica DMi8 THUNDERED microscope, Germany) with 10× magnification (region of interest = 1330 × 1330 μm^2) and analyzed using Ibidi Tube Formation AI Analysis (MetaVi Labs, TX, USA) and Fiji ImageJ software (1.53t, NIH, MD, USA) for number of branches and roundness/projected area, respectively.

Methods—Precision MP in a Rat Hindlimb Model: Animal surgery was performed at The Penn State Hershey Medical Center in concordance with an Institute Animal Care and Use Committee (IACUC) approved protocol (# 47941). Sprague–Dawley (SD) rats around the age of 12 weeks were used (Charles River, MA, USA). Male and female animals were alternatively selected for surgery to ensure that any sex-specific differences in the results would be minimized. Isoflurane was used to anesthetize rats, and the surgical site was shaved and prepped using betadine solution. On the inner aspect of each hindlimb, incisions were made to expose the femoral artery and vein and allowing for circumferential vessel dissection over a length of 15 mm. A 60 μm needle was used to create 15 MP at 1 mm intervals into the femoral artery and vein. The contralateral hindlimb was surgically manipulated similarly but without MP. Tested conditions were MP (*n* = 12 hindlimbs) and no MP (control; *n* = 12 hindlimbs). Three rats were used for each GHS-S, GHS-M, GHS-L, or bulk (control) hydrogel group. The GHS-S, GHS-M, GHS-L, and bulk (control) hydrogel scaffolds were prepared in a custom-made acrylic mold of 15 mm (length) × 10 mm (width) × 3 mm (thickness). The scaffolds were directly placed on the exposed femoral artery and vein. Buried absorbable sutures were used for skin closure. Rats were placed in individual cages and housed in a standard day/night light cycle environment with ad libitum food and water. Carprofen was used as a single one-time subcutaneous injection for pain control. Animals were euthanized on day 7 for further analysis.

Methods—Immunofluorescence Staining: Immunofluorescence staining was conducted to determine cellular infiltration in the scaffolds (*n* = 3 scaffolds per condition). Anti-CD31 and anti-F4/80 antibodies were used to detect endothelial cells and macrophages, respectively. To prepare the tissue slides for immunofluorescence, they were deparaffinized and rehydrated by immersion in xylene and ethanol, each two times for 10 min. Next, slides were immersed in ethanol 95 vol% for 5 min, followed by immersion in 70 and 50 vol% alcohol for 5 min. They were rinsed with deionized water and prepared for antibody staining, as previously described.[86] Secondary antibodies labeled with AlexaFluor 493 or 647 were used. Samples were mounted and DAPI counterstained with Fluroshield. Images were acquired using the EVOS FL Auto Imaging System (ThermoFisher Scientific, MA, USA). At least three images at 20× magnification (region of interest = 580.50 × 435.37 μm^2) were used from each group for the AI analysis.[89] Ibidi Tube Formation AI Analysis (MetaVi Labs, TX, USA) was used for CD31 quantification and vessel analysis. Labeled images were used to train the AI to detect large blood vessels. These multiple training sessions were completed with Ibidi prior to final analysis to ensure accurate vessel density measurements. The total tube length, average vessel diameter, number of branch points, and mean vascular density of the CD31 positively labeled cells were calculated (Figure S6, Supporting Information). The intercapillary distance and immune cell staining area were counted using the Fiji ImageJ software (1.53t, NIH, MD, USA).[90] A total of 24 animals, with six hindlimbs per group, were used for detailed analysis at day 7.

Methods—Demonstration of Perfusability: At day 7, in vivo perfusion assessment for *n* = 8 GHS-M per condition (MP or non-MP control) to provide at least 80% of calculable power to detect a standardized effect size (Cohen's *d*) of 1.60 with respect to the outcome of vascularization using a two-sided test having a significance level of 0.05. This was done using a previously described fluorescence vessel painting technique.[82] Under general anesthesia, an aortotomy was made just proximal to the iliac bifurcation. An olive-tipped catheter (Medtronic DLP 1.8" internal mammary artery Cannula, 1 mm tip, Dublin, Ireland) was then inserted and secured in place. The lower extremity vasculature was perfused with 50–100 mL of

37 °C PBS. The inferior vena cava was transected to allow outflow. After PBS flushing, the lower extremity vasculature was fixed by injecting 40 mL of 2.5 vol% glutaraldehyde solution. Adequate fixation was confirmed by the observation of nail bed pallor and stiffening of the rodent tail. Immediately after, each limb was perfused with carbocyanine. The lipophilic carbocyanine tracer, dissolved in ethanol (6 mg mL^{-1}) and stored at 4 °C as a 6.42 mM stock solution, was diluted 50 times in PBS, containing glucose (200 mM) to a final dye concentration of 0.128 mM just prior to infusion. Once again, adequate distal infusion of the vasculature was inferred by a pink color change in the hind nail beds and pink fluid extravasation from the transected inferior vena cava. Then, the scaffolds were explanted en bloc with the underlying femoral vessels. It was ensured to remove any adherent muscle fibers. The explants were placed between two glass slides and fixed in 10 wt% formalin for 48 h. Specimens were rinsed briefly in distilled water before being permanently mounted in the mounting medium and images were captured. For the AI analysis, five images were taken from each group at 10× magnification, and the region of interest was 1161.00 × 870.75 μm^2.

Methods—Histological Evaluation: At day 7, formalin-fixed tissue blocks of GHS-M and femoral artery and vein were used to obtain thin serial sections. Additionally, tissue samples from the liver, spleen, and kidney (*n* = 3 per condition) were collected from control and MP GHS-M groups. Subsequently, the sections underwent deparaffination and rehydration before being subjected to either H&E or Masson's trichrome (MT) staining. Blinded and random images of the control and MP sections were acquired by the EVOS FL Auto Imaging System (Thermo Fisher Scientific, Waltham, MA). The H&E-stained samples were assessed for normalcy by comparing them with the native rat liver, spleen, and kidney characteristics. For MT-stained samples, 40 high-powered field random images were analyzed to quantify RBC perfused luminal structures and total luminal structures. This quantification was performed by manual counting and further analyzed using the Fiji ImageJ software (1.53t, NIH, MD, USA).[90]

Methods—Statistical Analyses: To ensure the reliability and validity of the data, a large sample size, multiple measurement points, strict inclusion and exclusion criteria, and appropriate controls and blinding were used. The statistical analyses were performed using GraphPad Prism (9.5.0, San Diego, CA). We conducted the unpaired/paired two-tailed *t*-test or one-way/two-way analysis of variance (ANOVA) followed by the Tukey's or Holm–Šídák's posthoc multiple comparison test. The group size was calculated using G*Power software[91] (version 3.1.9.6) based on at least 80% power and probability of type I error of 0.05. All the data were acquired with at least three iterations (*n* ≥ 3). The levels of significance were stated with ns: non-significant, *p* > 0.05, **p* < 0.05, ***p* < 0.01, ****p* < 0.001, and *****p* < 0.0001.

Supporting Information

Supporting Information is available from the Wiley Online Library or from the author.

Acknowledgements

Conflict of Interest

The authors declare no conflict of interest.

Data Availability Statement

The data that support the findings of this study are available from the corresponding author upon reasonable request.

[1] M. J. Bosse, E. J. Mackenzie, J. F. Kellam, A. R. Burgess, L. X. Webb, M. F. Swiontkowski, R. W. Sanders, A. L. Jones, M. P. Mcandrew, B. M. Patterson, M. L. Mccarthy, T. G. Travison, R. C. Castillo, *N. Engl. J. Med.* **2002**, *347*, 1924.

[2] C. Karimkhani, R. P. Dellavalle, L. E. Coffeng, C. Flohr, R. J. Hay, S. M. Langan, E. O. Nsoesie, A. J. Ferrari, H. E. Erskine, J. I. Silverberg, T. Vos, M. Naghavi, *JAMA Dermatol.* **2017**, *153*, 406.

[3] D. L. Horn, J. Shen, E. Roberts, T. N. Wang, K. S. Li, G. E. O'keefe, J. Cuschieri, E. M. Bulger, B. R. H. Robinson, *J. Trauma Acute Care Surg.* **2020**, *89*, 186.

[4] R. W. Murphree, *Nurs. Clin. North Am.* **2017**, *52*, 405.

[5] C. Holmes, J. Wrobel, M. P. Mac Eachern, B. R. Boles, *Diabetes, Metab. Syndr. Obes.: Targets Ther.* **2013**, *6*, 17.

[6] F. Pallaske, A. Pallaske, K. Herklotz, J. Boese-Landgraf, *J. Wound Care* **2018**, *27*, 692.

[7] D. A. Banyard, J. M. Bourgeois, A. D. Widgerow, G. R. D. Evans, *Plast. Reconstr. Surg.* **2015**, *135*, 1740.

[8] J. J. Kim, G. R. D. Evans, *Clin. Plast. Surg.* **2012**, *39*, 359.

[9] H. Mehdizadeh, S. Sumo, E. S. Bayrak, E. M. Brey, A. Cinar, *Biomaterials* **2013**, *34*, 2875.

[10] E. Dantzer, F. M. Braye, *Br. J. Plast. Surg.* **2001**, *54*, 659.

[11] Y. F. Diehm, S. Fischer, E. Gazyakan, G. Hundeshagen, D. Kotsougiani-Fischer, F. Falkner, U. Kneser, C. Hirche, *J. Plast. Reconstr. Aesthetic Surg.* **2021**, *74*, 357.

[12] Z. Lokmic, G. M. Mitchell, *Tissue Eng., Part B* **2008**, *14*, 87.

[13] M. W. Laschke, B. Vollmar, M. D. Menger, *Tissue Eng., Part B* **2009**, *15*, 455.

[14] G. Hallock, *J. Reconstr. Microsurg.* **1988**, *4*, 155.

[15] K. K. Yap, G. C. Yeoh, W. A. Morrison, G. M. Mitchell, *Trends Biotechnol.* **2018**, *36*, 1011.

[16] Z. Lokmic, F. Stillaert, W. A. Morrison, E. W. Thompson, G. M. Mitchell, *FASEB J.* **2007**, *21*, 511.

[17] J. Rnjak-Kovacina, Y.-W. Gerrand, L. S. Wray, B. Tan, H. Joukhdar, D. L. Kaplan, W. A. Morrison, G. M. Mitchell, *Adv. Healthcare Mater.* **2019**, *8*, 1901106.

[18] W. Zhang, L. S. Wray, J. Rnjak-Kovacina, L. Xu, D. Zou, S. Wang, M. Zhang, J. Dong, G. Li, D. L. Kaplan, X. Jiang, *Biomaterials* **2015**, *56*, 68.

[19] J. Rnjak-Kovacina, L. S. Wray, J. M. Golinski, D. L. Kaplan, *Adv. Funct. Mater.* **2014**, *24*, 2188.

[20] Y.-I. Shen, H. Cho, A. E. Papa, J. A. Burke, X. Y. Chan, E. J. Duh, S. Gerecht, *Biomaterials* **2016**, *102*, 107.

[21] A. L. Torres, S. J. Bidarra, M. T. Pinto, P. C. Aguiar, E. A. Silva, C. C. Barrias, *Biomaterials* **2018**, *154*, 34.

[22] A. L. Torres, S. J. Bidarra, D. P. Vasconcelos, J. N. Barbosa, E. A. Silva, D. S. Nascimento, C. C. Barrias, *Biomaterials* **2020**, *228*, 119554.

[23] A. M. Kong, K. K. Yap, S. Y. Lim, D. Marre, A. Pébay, Y.-W. Gerrand, J. G. Lees, J. A. Palmer, W. A. Morrison, G. M. Mitchell, *Acta Biomater.* **2019**, *94*, 281.

[24] A. A. Szklanny, M. Machour, I. Redenski, V. Chochola, I. Goldfracht, B. Kaplan, M. Epshtein, H. Simaan Yameen, U. Merdler, A. Feinberg, D. Seliktar, N. Korin, J. Jaros, S. Levenberg, *Adv. Mater.* **2021**, *33*, 2102661.

[25] T. Takebe, K. Sekine, M. Enomura, H. Koike, M. Kimura, T. Ogaeri, R.-R. Zhang, Y. Ueno, Y.-W. Zheng, N. Koike, S. Aoyama, Y. Adachi, H. Taniguchi, *Nature* **2013**, *499*, 481.

[26] A. Lesman, J. Koffler, R. Atlas, Y. J. Blinder, Z. Kam, S. Levenberg, *Biomaterials* **2011**, *32*, 7856.

[27] B. Zohar, L. Debbi, M. Machour, N. Nachum, I. Redenski, M. Epshtein, N. Korin, S. Levenberg, *Acta Biomater.* **2023**, *163*, 182.

[28] J. Fu, C. Wiraja, H. B. Muhammad, C. Xu, D.-A. Wang, *Acta Biomater.* **2017**, *58*, 225.

[29] L. Debbi, B. Zohar, M. Shuhmaher, Y. Shandalov, I. Goldfracht, S. Levenberg, *Biomaterials* **2022**, *280*, 121286.

[30] C. M. Franca, A. Athirasala, R. Subbiah, A. Tahayeri, P. Selvakumar, A. Mansoorifar, S. Horsophonphong, A. Sercia, L. Nih, L. E. Bertassoni, *Adv. Healthcare Mater.* **2023**, *12*, 2202840.

[31] P. C. Hancock, S. V. Koduru, M. Sun, D. J. Ravnic, *Microvasc. Res.* **2021**, *134*, 104121.

[32] J. Rouwkema, N. C. Rivron, C. A. Van Blitterswijk, *Trends Biotechnol.* **2008**, *26*, 434.

[33] L.-J. Chen, H. Kaji, *Lab Chip* **2017**, *17*, 4186.

[34] A. Sheikhi, J. De Rutte, R. Haghniaz, O. Akouissi, A. Sohrabi, D. Di Carlo, A. Khademhosseini, *Biomaterials* **2019**, *192*, 560.

[35] Z. Ataie, S. Kheirabadi, J. W. Zhang, A. Kedzierski, C. Petrosky, R. Jiang, C. Vollberg, A. Sheikhi, *Small* **2022**, *18*, 2202390.

[36] A. C. Daly, L. Riley, T. Segura, J. A. Burdick, *Nat. Rev. Mater.* **2020**, *5*, 20.

[37] L. Riley, L. Schirmer, T. Segura, *Curr. Opin. Biotechnol.* **2019**, *60*, 1.

[38] Y. Kang, J. Chang, *Regener. Med.* **2018**, *13*, 705.

[39] P. Xia, Y. Luo, *J. Biomed. Mater. Res., Part B* **2022**, *110*, 1206.

[40] Y.-C. Chiu, M.-H. Cheng, H. Engel, S.-W. Kao, J. C. Larson, S. Gupta, E. M. Brey, *Biomaterials* **2011**, *32*, 6045.

[41] T. H. Qazi, L. Tytgat, P. Dubruel, G. N. Duda, S. Van Vlierberghe, S. Geissler, *ACS Biomater. Sci. Eng.* **2019**, *5*, 5348.

[42] L. Zieber, S. Or, E. Ruvinov, S. Cohen, *Biofabrication* **2014**, *6*, 024102.

[43] F. Bai, Z. Wang, J. Lu, J. Liu, G. Chen, R. Lv, J. Wang, K. Lin, J. Zhang, X. Huang, *Tissue Eng., Part A* **2010**, *16*, 3791.

[44] T. Yu, Q. Liu, T. Jiang, X. Wang, Y. Yang, Y. Kang, *Adv. Funct. Mater.* **2016**, *26*, 6719.

[45] D. B. Kolesky, K. A. Homan, M. A. Skylar-Scott, J. A. Lewis, *Proc. Natl. Acad. Sci. USA* **2016**, *113*, 3179.

[46] L. Shao, Q. Gao, C. Xie, J. Fu, M. Xiang, Y. He, *Biofabrication* **2020**, *12*, 035014.

[47] S. I. Somo, B. Akar, E. S. Bayrak, J. C. Larson, A. A. Appel, H. Mehdizadeh, A. Cinar, E. M. Brey, *Tissue Eng., Part C* **2015**, *21*, 773.

[48] T. H. Qazi, J. Wu, V. G. Muir, S. Weintraub, S. E. Gullbrand, D. Lee, D. Issadore, J. A. Burdick, *Adv. Mater.* **2022**, *34*, 2109194.

[49] K. L. Wilson, S. C. L. Pérez, M. M. Naffaa, S. H. Kelly, T. Segura, *Adv. Mater.* **2022**, *34*, 2201921.

[50] D. R. Griffin, W. M. Weaver, P. O. Scumpia, D. Di Carlo, T. Segura, *Nat. Mater.* **2015**, *14*, 737.

[51] D. R. Griffin, M. M. Archang, C.-H. Kuan, W. M. Weaver, J. S. Weinstein, A. C. Feng, A. Ruccia, E. Sideris, V. Ragkousis, J. Koh, M. V. Plikus, D. Di Carlo, T. Segura, P. O. Scumpia, *Nat. Mater.* **2021**, *20*, 560.

[52] L. J. Pruett, C. H. Jenkins, N. S. Singh, K. J. Catallo, D. R. Griffin, *Adv. Funct. Mater.* **2021**, *31*, 2104337.

[53] L. R. Nih, E. Sideris, S. T. Carmichael, T. Segura, *Adv. Mater.* **2017**, *29*, 1606471.

[54] J. Fang, J. Koh, Q. Fang, H. Qiu, M. M. Archang, M. M. Hasani-Sadrabadi, H. Miwa, X. Zhong, R. Sievers, D.-W. Gao, R. Lee, D. Di Carlo, S. Li, *Adv. Funct. Mater.* **2020**, *30*, 2004307.

[55] J. Koh, D. R. Griffin, M. M. Archang, A.-C. Feng, T. Horn, M. Margolis, D. Zalazar, T. Segura, P. O. Scumpia, D. Di Carlo, *Small* **2019**, *15*, 1903147.

[56] A. Sheikhi, J. de Rutte, R. Haghniaz, O. Akouissi, A. Sohrabi, D. Di Carlo, A. Khademhosseini, *MethodsX* **2019**, *6*, 1747.

[57] N. Zoratto, D. Di Lisa, J. De Rutte, M. N. Sakib, A. R. Alves E Silva, A. Tamayol, D. Di Carlo, A. Khademhosseini, A. Sheikhi, *Bioeng. Transl. Med.* **2020**, *5*, e10180.

[58] C.-C. Hua, X.-M. Liu, L.-R. Liang, L.-F. Wang, J.-C. Zhong, *Front. Cardiovasc. Med.* **2022**, *8*, 784044.

[59] J. M. de Rutte, J. Koh, D. Di Carlo, *Adv. Funct. Mater.* **2019**, *29*, 1900071.

[60] K. Yue, G. Trujillo-De Santiago, M. M. Alvarez, A. Tamayol, N. Annabi, A. Khademhosseini, *Biomaterials* **2015**, *73*, 254.

[61] Y. Wang, R. K. Kankala, C. Ou, A. Chen, Z. Yang, *Bioact. Mater.* **2022**, *9*, 198.

[62] R. W. Barrs, J. Jia, S. E. Silver, M. Yost, Y. Mei, *Chem. Rev.* **2020**, *120*, 10887.

[63] K. Yue, X. Li, K. Schrobback, A. Sheikhi, N. Annabi, J. Leijten, W. Zhang, Y. S. Zhang, D. W. Hutmacher, T. J. Klein, A. Khademhosseini, *Biomaterials* **2017**, *139*, 163.

[64] Y. Zhang, P. Kumar, S. Lv, D. Xiong, H. Zhao, Z. Cai, X. Zhao, *Mater. Des.* **2021**, *199*, 109398.

[65] H. Bae, A. F. Ahari, H. Shin, J. W. Nichol, C. B. Hutson, M. Masaeli, S.-H. Kim, S. Yamanlar, A. Khademhosseini, *Soft Matter* **2011**, *7*, 1903.

[66] H. Aubin, J. W. Nichol, C. B. Hutson, H. Bae, A. L. Sieminski, D. M. Cropek, P. Akhyari, A. Khademhosseini, *Biomaterials* **2010**, *31*, 6941.

[67] J. Ramón-Azcón, S. Ahadian, R. Obregón, G. Camci-Unal, S. Ostrovidov, V. Hosseini, H. Kaji, K. Ino, H. Shiku, A. Khademhosseini, T. Matsue, *Lab Chip* **2012**, *12*, 2959.

[68] S. Lee, J. De Rutte, R. Dimatteo, D. Koo, D. Di Carlo, *ACS Nano* **2022**, *16*, 38.

[69] S. Han, H. M. Sun, K.-C. Hwang, S.-W. Kim, *Crit. Rev. Eukaryotic Gene Expression* **2015**, *25*, 145.

[70] Sigma-Aldrich, FITC-labelled polysaccharides, https://www.sigmaaldrich.com/technical-documents/articles/chemistry/fluorescently-labeled-dextrane.html, n.d. (accessed: April 2022).

[71] C. F. Guimarães, L. Gasperini, A. P. Marques, R. L. Reis, *Nat. Rev. Mater.* **2020**, *5*, 351.

[72] S. Budday, T. C. Ovaert, G. A. Holzapfel, P. Steinmann, E. Kuhl, *Arch. Comput. Methods Eng.* **2020**, *27*, 1187.

[73] A. Forghani, S. V. Koduru, C. Chen, A. N. Leberfinger, D. J. Ravnic, D. J. Hayes, *Regener. Eng. Transl. Med.* **2020**, *6*, 101.

[74] J. G. Maijub, N. L. Boyd, J. R. Dale, J. B. Hoying, M. E. Morris, S. K. Williams, *Cell Transplant.* **2015**, *24*, 2029.

[75] A. C. Newman, C. C. W. Hughes, *Vasc. Cell* **2012**, *4*, 13.

[76] S. J. Leibovich, P. J. Polverini, H. M. Shepard, D. M. Wiseman, V. Shively, N. Nuseir, *Nature* **1987**, *329*, 630.

[77] L. Bingle, C. E. Lewis, K. P. Corke, M. W. R. Reed, N. J. Brown, *Br. J. Cancer* **2006**, *94*, 101.

[78] F. Krombach, S. Münzing, A. M. Allmeling, J. T. Gerlach, J. Behr, M. Dörger, *Environ. Health Perspect.* **1997**, *105*, 1261.

[79] M. Félétou, in *Colloquium Series on Integrated Systems Physiology: From Molecule to Function to Disease* (Eds: D. N. Granger, J. P. Granger), Vol. *3*, Morgan & Claypool Life Sciences, San Rafael, CA **2011**.

[80] J. M. Lowen, G. C. Bond, K. H. Griffin, N. K. Shimamoto, V. L. Thai, J. K. Leach, *Adv. Healthcare Mater.* **2023**, *12*, 2202239.

[81] Y. Liu, A. Suarez-Arnedo, L. Riley, T. Miley, J. Xia, T. Segura, *Adv. Healthcare Mater.* **2023**, *12*, 2300823.

[82] D. Ravnic, X. Jiang, T. Wolloscheck, J. Pratt, H. Huss, S. Mentzer, M. Konerding, *Microvasc. Res.* **2005**, *70*, 90.

[83] A. S. Chung, N. Ferrara, *Annu. Rev. Cell Dev. Biol.* **2011**, *27*, 563.

[84] KMPR 1000, Kayaku Advanced Materials, Inc, https://kayakuam.com/products/kmpr-1000/, n.d. (accessed: March 2022).

[85] Z. Ataie, A. Jaberi, S. Kheirabadi, A. Risbud, A. Sheikhi, *J. Vis. Exp.* **2022**, *190*, e64829.

[86] S. V. Koduru, A. N. Leberfinger, I. T. Ozbolat, D. J. Ravnic, *Stem Cells Dev.* **2021**, *30*, 1153.

[87] P. A. Zuk, M. Zhu, H. Mizuno, J. Huang, J. W. Futrell, A. J. Katz, P. Benhaim, H. P. Lorenz, M. H. Hedrick, *Tissue Eng.* **2001**, *7*, 211.

[88] P. A. Zuk, M. Zhu, P. Ashjian, D. A. De Ugarte, J. I. Huang, H. Mizuno, Z. C. Alfonso, J. K. Fraser, P. Benhaim, M. H. Hedrick, *Mol. Biol. Cell* **2002**, *13*, 4279.

[89] T. T. Hormel, T. S. Hwang, S. T. Bailey, D. J. Wilson, D. Huang, Y. Jia, *Prog. Retinal Eye Res.* **2021**, *85*, 100965.

[90] J. Schindelin, I. Arganda-Carreras, E. Frise, V. Kaynig, M. Longair, T. Pietzsch, S. Preibisch, C. Rueden, S. Saalfeld, B. Schmid, J.-Y. Tinevez, D. J. White, V. Hartenstein, K. Eliceiri, P. Tomancak, A. Cardona, *Nat. Methods* **2012**, *9*, 676.

[91] F. Faul, E. Erdfelder, A.-G. Lang, A. Buchner, *Behav. Res. Methods* **2007**, *39*, 175.